ACS APPLIED ENERGY MATERIALS

www.acsaem.org Article

# Correlating Processing Conditions to Short- and Long-Range Order in Coating and Drying Lithium-Ion Batteries

Renee M. Saraka, Samantha L. Morelly, Maureen H. Tang, and Nicolas J. Alvarez*

Cite This: *ACS Appl. Energy Mater.* 2020, 3, 11681−11689 Read Online

ACCESS | Metrics & More | Article Recommendations | Supporting Information

**ABSTRACT:** Processing conditions of battery slurries into electrodes are known to affect final battery performance. However, there is a lack of fundamental understanding of how the relationships between processing conditions, the slurry microstructure, and the film microstructure affect electrode performance. This study determines the effects of the coating shear rate and drying temperature on battery electrode performance via discharge capacity. We use rheological measurements and energy dispersive X-ray spectroscopy (EDS) to correlate slurry and electrode microstructures to trends in discharge capacity. The radial distribution function is used to quantify differences in the electrode microstructure. More specifically, we show that the correlation between carbon and active material EDS detections to be the most relevant in understanding battery performance. Electrodes with both short- and long-range carbon/active material orders have the highest discharge capacities. This microstructure can be obtained through high shear rates, which induce better carbon dispersion via strong hydrodynamic forces, or through high temperature drying by preventing unwanted time-dependent structural changes after flow cessation. This analysis provides concrete evidence for the importance of both short-range and long-range contacts between the conductive additive and active material on battery performance.

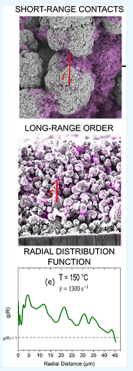


**KEYWORDS:** *electrode manufacturing, shear effects, drying effects, battery slurry rheology, radial-distribution function, lithium-ion battery*



## 1. INTRODUCTION

As lithium ion batteries power the growing market of consumer electronics and electric vehicles, researchers continue to focus on increasing the battery energy density. Although advanced materials continue to improve theoretical capacity limits, optimization ultimately requires processing technology to achieve fast, homogeneous ion and electron transport. There is growing consensus that the performance of battery electrodes with industrially relevant carbon concentrations (<5 wt %) is effectively controlled by electron transport.[1−5] Efficient electron transport is directly related to the structure and connectivity between the three components, that is, the active material, conductive additive, and polymer binder.[6,7] The electrode microstructure and connectivity in turn strongly depend on the electrode slurry mixing, coating, and drying processes.[2,3,8−15] Previously, we showed how slurry mixing impacts the short-range electronic contacts that control electrode rate capability.[1] However, slurry coating and drying also are known to impact performance. Relating these processes to the electrode microstructure, particularly electronic connectivity, is necessary for further insight and improvements to electrode manufacturing. Several experimental and theoretical studies have shown the impact of drying temperature on the distribution of the polymer binder. The solvent removal process has been modeled[16] and studied experimentally. In graphite anodes, researchers have found that binder accumulates at the surface of the anode with higher drying temperature, consequently depleting the binder at the current collector resulting in poor adhesion.[17−19] Müller et al. showed via EDS image analysis that higher temperatures lead to higher binder concentration at the electrode's top surface, which results in reduced adhesion strength between the electrode and current collector.[17] Subsequently, Westphal and Kwade suggested to avoid drying-induced segregation of the polymer binder via a soft drying temperature of 80 °C to improve mechanical elasticity and relative electrode resistance.[18] Furthermore, Jaiser et al. suggest that lower drying temperatures result in an ideal, homogeneous binder distribution that provides higher discharge capacities.[19] These studies suggest that the distribution of binder is essential in ensuring adhesion to the current collector. While binder is an essential component, it is a nonconductive additive and is studied in the anode, which is not typically capacity limiting. Fewer studies have addressed the effect of drying temperature on the conductive carbon distribution in cathode electrodes, which could lead to more rational capacity optimization.

The applied shear rate during coating is arguably important for proper dispersion of the components in the final electrode film. Few studies have directly examined the effect of shear on electrode performance. However, some studies have reported

**Received:** July 20, 2020
**Accepted:** November 2, 2020
**Published:** November 30, 2020

the effect of shear on physical properties of electrodes in order to maximize the area of the useful electrode film.[14,20,21] For example, Bitsch et al. utilized capillary suspensions to improve electrodes at low shear and keep slurry viscosity constant at high shear. The additives used in their study decreased capillary spreading, decreased the area affected by edge effects, and increased the coating edge thickness.[14] Using slot die coating, the authors also conclude that increasing the shear rate increased the coating edge thickness.[20] It is well-known that slot-die coated films outperform doctor blade coated electrodes. One explanation for this is the difference in shear rates. Slot die coating achieves shear rates on the order $10^3$ $s^{-1}$ and shear strains of order 10.[20] However, the effect of shear still needs to be quantified.

The electrode microstructure is expected to be a strong function of the shear applied during coating. Industrially relevant battery slurries form colloidal gels in the absence of dry-mixing.[1,22] There is a well-characterized nonlinear dependence of the colloidal gel microstructure on the applied shear rate.[23−26] Eberle et al. showed that hydrodynamic forces induced in situ cluster reorganization depending on the applied shear rate, suggesting that shear rates of sufficient magnitude will increase particle dispersion and connectivity during film formation.[24] Furthermore, Colombo et al. evaluated the evolution of the colloidal gel microstructure after low shear, suggesting that selective aggregate breakdown is occurring even with extremely low shear rates.[26] In contrast, Varadan and Solomon showed that their colloidal gel showed no changes in aggregate size at shear rates of 120 $s^{-1}$, especially close to the gel point temperature.[27] These conflicting results clearly show that shear-induced changes in the microstructure depend on the type of gel and the magnitude of the shear rate.

The drying time is also expected to influence the electrode structure after the cessation of shear. This is supported by the literature that shows colloidal systems undergo aging and recovery after flow cessation.[26−31] The mechanism for aging is thought to arise from particle rearrangements caused by hydrodynamic shear forces.[28] For example, Gordon et al. showed that colloidal gels show faster structural recovery (measured via elastic modulus) for higher imposed stresses.[28] This is supported by another study that shows a delay in the relaxation of the colloidal microstructure due to changes in the network density during the applied shear flow.[29] The evolution of the colloidal microstructure during shear and drying have not been explicitly tied to battery electrodes during processing.

We recently showed that improved electrode performance for carbon-starved slurry formulations is achieved via dry-mixing carbon black (CB) with an active material prior to wet-mixing. The dry-mixing induces short-range contacts between carbon and the active material to achieve improved electron transport.[1] One important question that remains is whether shear and temperature during processing can improve carbon and active material connectivity without dry-mixing. This study examines the combinatorial effect of the shear rate and drying temperature on battery performance. Shear rates from 300 to 1300 $s^{-1}$ and drying temperatures between 23 and 150 °C are applied to the same colloidal gel slurry formulation. These shear rates are intended to span low shear rates typical in laboratory studies and shear rates achieved in slot-die coating. The dried films are compressed, made into a battery, and tested for rate capability. As expected, electrode performance is a strong function of the drying temperature and shear rate.

Scanning electron microscopy (SEM) and EDS maps are studied to correlate battery performance to component distribution in cross-sectional images of the electrode films through a radial distribution function. The radial distribution function defines the probability of finding a molecule at a radial distance from another molecule of interest. It is historically used to understand interactions between molecules in solids, liquids, and gases, for example, defining order in crystalline lattice structures. We propose that the radial distribution function applied to EDS maps can be used to quantify short-range and long-range pathways between carbon and the active material. Furthermore, we show that there are direct correlations between short-/long-range pathways and electrode performance.

## 2. METHODS

**2.1. Electrode Film Composition and Mixing.** Electrode films were made with 95 wt % active material of $LiNi_{0.33}Mn_{0.33}Co_{0.33}O_2$ (NMC) (Toda America, NM3100) with an average particle size of 10 $\mu$m and a Brunauer−Emmett−Teller (BET) area of 0.5 $m^2/g$. Conductive additive consisting of 2.5 wt % CB (MTI, Super C65) with a BET area of 62.6 $m^2/g$ was used. The active material and conductive additive were added to a solution of 2.5 wt % polyvinylidene difluoride (PVDF) (Arkema, MW = 380k) in 3.405 mL of 1-methyl-2-pyrrolidinone (NMP), which was mixed separately in a Thinky planetary mixer at 1800 rpm for 10 min. The PVDF solution and particles were combined and mixed in the same device for 7.5 min at 1800 rpm. The final slurry composition remained constant through all trials at 95% active material, 2.5% CB, and 2.5% PVDF binder.

**2.2. Electrode Film Coating and Drying.** Slurries were coated onto an aluminum current collector via an automatic coater with a doctor blade attachment of depth 4.33 mm (0.17 in.) and 150 mm coating width (TOB Energy, TOB-TM300). Coating speeds are adjustable between 0 and 100 mm/s with an accuracy of 10 mm/s. The doctor blade has an adjustable coating thickness between 0.01 and 3.5 mm. The coating thickness was constant for all studies at 0.1 mm, resulting in a constant shear strain, $\gamma = 43.3$. This strain is a result of the gap height (coating thickness) and the width of the doctor blade used to coat the film. Because it is important to control film thickness for similar ion transport between films, the induced shear strain was fixed for all coatings. The magnitude of strain used in this study is on the same order of magnitude as slot-die coating setups. Shear rates were measured using video analysis. Films were coated at 300, 750, and 1300 $s^{-1}$, then either placed in a fume hood to dry overnight at room temperature, at 80 °C using the coater's oven attachment, or at 150 °C using an in-house controlled hot plate setup. Visual inspection showed drying times of >8 h, 2 h, and 5 min, respectively.

**2.3. Electrode Preparation and Assembly.** After the initial drying time, all films were further vacuum-dried at 120 °C for 12 h, then punched into 3/8″ diameter electrodes. Individual electrodes were compressed at 20 MPa to ensure adequate substrate adhesion using a Carver melt press at room temperature. Standard size 2032 half cells were fabricated in an argon atmosphere glove box with lithium metal counter electrodes, two Celgard separators, and an LP30 electrolyte (Gotion).

**2.4. Testing.** *2.4.1. Rheological Measurements.* Amplitude sweeps were measured from 0.1 to 10% strain and frequency sweeps were measured between 0.1 and 100 rad/s at 0.1% strain on an ARES G2 (TA Instruments) rheometer. Only slurries exhibiting reproducible rheology after mixing were cast into films. Additional frequency sweeps using a DHR-3 (TA Instruments) were taken after applied shear. To mimic the shear flow during coating, steady shear rates were applied with a 40 mm parallel plate geometry at 300, 750, and 1300 $s^{-1}$ for 10, 7, and 3 s, respectively. Microstructure relaxation experiments were conducted via frequency sweeps from 0.1 to 100


https://dx.doi.org/10.1021/acsaem.0c01305
ACS Appl. Energy Mater. 2020, 3, 11681−11689

rad/s at 0.1% strain measured 0, 1, and 2 h after constant shear rate experiments.

*2.4.2. Conditioning and Rate Capability Testing.* Electrochemical testing was completed using an Arbin battery cycler (Arbin Instruments). All cells were conditioned by completing four cycles at a rate of 0.1 C ranging between 4.3 and 3.0 V. After conditioning, cells completed four cycles discharging at 0.5 C, 1 C, 2 C, 5 C, 10 C, then a final 0.5 C. All charging cycles were performed at a constant 0.1 C.

*2.4.3. Microscopic Imaging and Analysis.* SEM images (FEI Quanta 600 ESEM) and energy dispersive spectroscopy (EDS) maps (EDAX Team) were measured (20 kV) on the same films used for battery testing. The SEM and EDS images were collected on the same region of interest and analyzed to determine component distributions. The samples were prepared by vertically slicing electrodes in half with a razor blade. The half of the electrode was then mounted to a 90° angle SEM stub with a conductive carbon tape, exposing the exposed cross section. Previous work by our group studied SEM sample prep methods and showed that slicing from the top to bottom or bottom to top does not cause measurable smearing of elements.[32] Cross section polishing was not used to prevent altering element distribution. SEM/EDS images were cropped to only include the electrode cross section. EDS imaging provides spatially evolved elemental analysis from areas as small as 1 nm. EDS works by applying high voltage energy to a conductive sample which causes inner shell electrons to transition to a higher energy level and emit X-rays with characteristic energy of the probed element. Thus, elements are identified by a peak energy.[33] 20 kV excitation was chosen for this study, which is 2.5 times greater than the highest elemental $K_\alpha$ of nickel, 7.471 keV. EDS signals for carbon (C), fluorine (F), aluminum (Al), nickel (Ni), cobalt (Co), manganese (Mn), and oxygen (O) were detected during testing. For this study, we will focus on the spatial distributions of C detections as an indicator for the conductive additive and Mn as an indicator for the active material.

SEM and EDS images are a result of a large depth-of-field, which leads to a three-dimensional (3D)-like imaging of the electrode cross-section surface. For simplicity, we developed a routine to reduce the 3D EDS maps to two-dimensional (2D) planar elemental maps. The 3D image is dissected into planes of detection intensity and reduced to a 2D map of pixels with a set intensity range. More specifically, a pixel intensity histogram was created for each EDS image. A distinct population with the highest pixel intensity is considered to represent the top layer, that is, the brighter the pixel intensity the closer its proximity to the detector. The image was reduced to only include pixels in the highest pixel intensity population. Using the reduced image, the radial distribution function was calculated to coordinate the location of carbon or manganese pixel detections. That is, nonblack pixels in the respective EDS map, to all other carbon or manganese detections within a given radius, $r$. The 2D radial distribution function, $g(r)$, is given by

$$g(r) = \frac{H(r)}{N\rho\pi[(r + \Delta r)^2 - r^2]}$$

where $r$ is the radial distance, $H(r)$, is the pair correlation histogram normalized by the 2D particle density, $\rho = N/L^2$, and the number of detections, $N$, where $L$ is the radial length of the box given by $L^2 = (L_x^2 + L_y^2)$.[34]

## 3. RESULTS AND DISCUSSION

The rate capabilities of electrodes with variable coating shear and drying temperature are shown in Figure 1a–d. Each data point represents the average discharge capacity of three to four electrodes with four cycles each (an average of 12–16 capacities per C-rate). Error bars represent one standard deviation of the 9–12 data points. A full account of the cycles contributing to one average value is shown in Figure S1. Consistent with expectations, all electrodes approach the theoretical capacity at 0.1 C, while capacity at rates 2 C and greater are significantly reduced. For electrodes dried at the lowest temperature of 23 °C (Figure 1a), discharge capacity increases monotonically with the shear rate. At the highest drying temperature of 150 °C (Figure 1b), very little effect of the shear rate is observed. Figure 1a,b suggest better electrodes result from high shear rates and high temperatures.

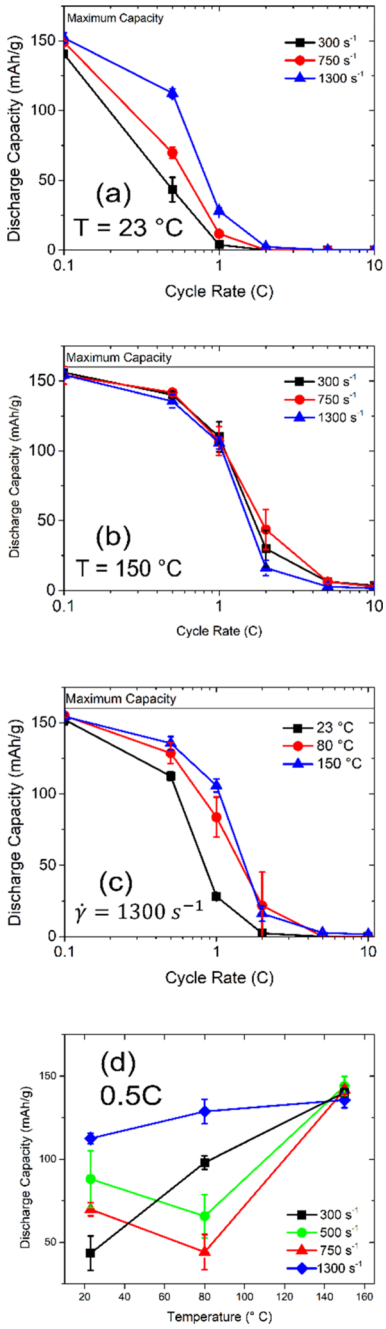


**Figure 1.** Rate capability results for (a) 23 °C drying shows low discharge capacities that decrease with the decreasing shear rate (b) 150 °C samples show nearly identical discharge capacities with varying shear, suggesting the importance of temperature (c) 1300 $s^{-1}$ results in high discharge capacities that improve slightly with increasing temperature with minimal variance within each sample set (d) a summary of all discharge capacities at 0.5 C show the best performance at 1300 $s^{-1}$ and 150 °C.

Figure 1c compares the discharge capacities at high shear rates (1300 $s^{-1}$) for films coated at three temperatures. There is an increase in the discharge capacity with increasing


https://dx.doi.org/10.1021/acsaem.0c01305
ACS Appl. Energy Mater. 2020, 3, 11681–11689

temperature. At this shear rate, the differences between discharge capacities is significantly smaller than other rates, for example, a decrease of 20 mA h/g at 1 C compared to Figure 1a, which shows a decrease of 70 mA h/g. Overall at 1 C and high shear rates, the intermediate and high temperature samples show relatively high discharge capacity compared to low shear rates, see Figure 1a. At 1 C, low temperature drying shows a much more significant drop in discharge capacity, suggesting the importance of fast drying. A comparison of Figure 1b,c suggest that electrode performance is significantly more sensitive to drying temperature than the shear rate. Figure 1d summarizes the findings by comparing the discharge capacity at 0.5 C for all conditions. At low shear rates (black line), the discharge capacity increases monotonically with increasing drying temperature. Intermediate shear rates (red line) show a surprising nonmonotonic increase in battery performance with increasing temperature; a minimum in discharge capacity is achieved at 80 °C. An additional study at 500 $s^{-1}$ (green line) was conducted to validate the minimum. High shear rates (blue line) exhibit high discharge capacities, and have significantly less variation with temperature. It is clear from Figure 1d that high shear rates allow for high discharge capacities at any temperature. This shear rate is on the same order of magnitude as that applied during slot die coating,[20] which is a process known to make better performing electrodes. The highest temperature shows a constant high discharge capacity. There are many possible factors that contribute to the observed capacity differences. It is important to consider physical properties of the electrodes as well as processing-induced changes.

It is well-known that ion and electron transport are faster in thinner electrodes, while ion transport increases with porosity. For low-carbon formulations such as the systems here, lower porosity is expected to yield better performance. Figure 2a shows that thickness is unable to describe all of the trends in electrode performance. Although all electrodes in this work were coated with a constant doctor blade height of 100 $\mu$m, Figure 2 shows that the final film thickness and porosity strongly vary with the applied shear rate and drying temperature. One possible explanation for film thicknesses greater than 100 $\mu$m is due to an increased wet film thickness caused by lubrication forces during coating.[34] There are significant outliers to the expected trend with thickness. For example, boxes 1 and 2 in Figure 2a represent electrodes fabricated at 23 °C and dried at 750 and 300 $s^{-1}$, respectively. The differences in porosity and thickness are ±20% and ±10 $\mu$m, however, the difference in capacity is significant, 43 mA h/g, or 30% lower for box 2 at 0.5 C. Boxes 1 and 3 represent different shear rates as well as different temperatures. The difference in porosity and thickness are ±20% and 10 $\mu$m, respectively, however, the capacity loss is much greater than expected (70 mA h/g). Furthermore, Figure 2b clearly shows that ion transport is not limiting electrode performance. Circles 1 and 2 have very similar discharge capacities (140−130 mA h/g) but different thicknesses (95−120 $\mu$m) and porosity (25% lower). Overall, although variations in thickness and porosity certainly impact the overall electrode performance, they do not account for all of the variations in the discharge capacity. Further analysis of the electrode microstructure is needed to determine how shear and drying impact local connections between particles.

SEM and EDS imaging of electrode cross sections were used to gain insight into the electrode microstructure. SEM images

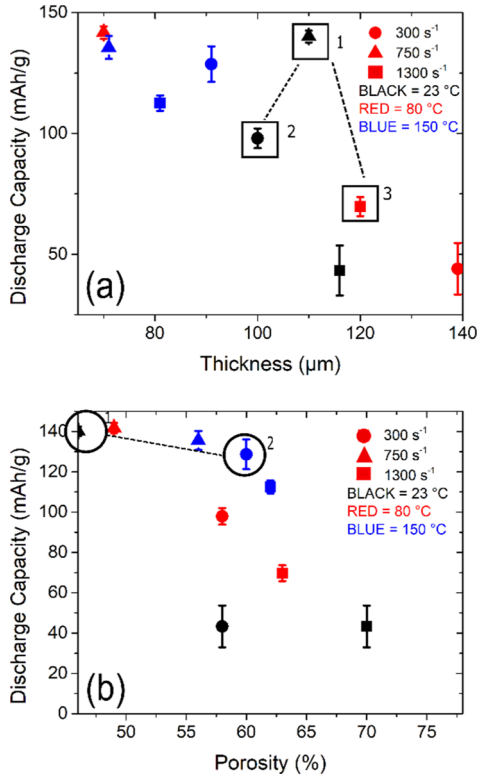


**Figure 2.** Thickness (a) and porosity (b) cannot simply explain the discharge capacity as proofed by differences between boxes 1, 2, and 3 and similarities between circles 1 and 2.

give a general overview of the particle packing and distribution in the electrode, while EDS maps show the elemental distribution. Two sample SEM and EDS maps are shown in Figure 3. SEM samples, shown in Figure 3a,d were prepared with previously validated methods to prevent element smearing and distribution alteration. Figure 3a−c correspond to a film processed at 300 $s^{-1}$ and dried at 23 °C. Figure 3d−f corresponds to a film processed at 1300 $s^{-1}$ and dried at 23 °C. Recall that the higher shear rate sample (Figure 3d−f) has significantly higher discharge capacity. Manganese (Mn) maps in Figure 3b,e appear to be uniform and consistent for both electrode films, while carbon maps in Figure 3c,f show qualitative differences in carbon dispersion and connectivity.

It is well-understood that conductive additive is necessary to transport electrons to and from the surface of active material particles to complete the electrochemical reaction. Therefore, discharge capacity is expected to strongly depend on how connected a given active particle surface is to the carbon filling interstitial sites ("short-range contacts") and how well the interstitial carbon is connected to the current collector ("long-range contacts"). Our previous results argue that neither long-range carbon connectivity, nor short-range contacts alone are enough to ensure good battery performance. Rather, both long- and short-range contacts must be present and form a continuous carbon network from the surface of the active particles to the current collector. To quantify these long- and short-range contacts, we utilized a radial distribution function analysis to perform correlations of the locations of manganese pixels to carbon pixels (Mn/C), and carbon pixels to other carbon (C/C) pixels. The aim is to correlate elemental distribution in the battery electrode to battery performance. Mn was arbitrarily chosen as a representative signal of the


https://dx.doi.org/10.1021/acsaem.0c01305
ACS Appl. Energy Mater. 2020, 3, 11681−11689

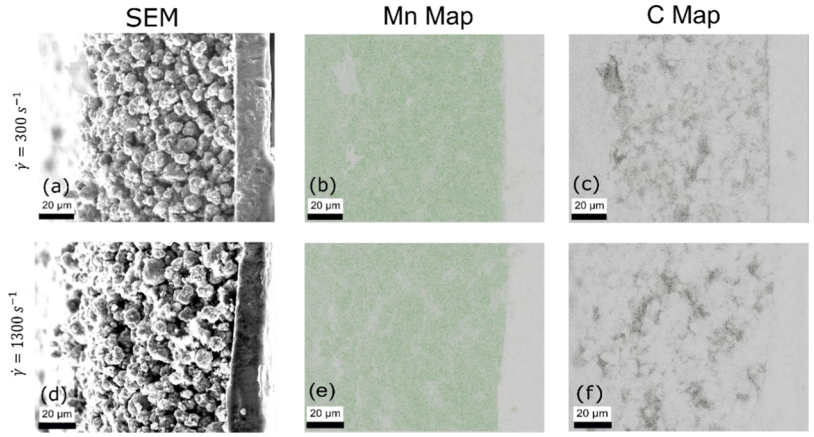


**Figure 3.** SEM and EDS images (a) 23 °C, 300 $s^{-1}$ electrode image (b) 23 °C, 300 $s^{-1}$ manganese map is uniform with small open pockets (c) 23 °C, 300 $s^{-1}$ carbon map shows a sporadic C distribution (d) 23 °C, 1300 $s^{-1}$ electrode image (e) 23 °C, 1300 $s^{-1}$ manganese map is homogenous (f) 23 °C, 300 $s^{-1}$ carbon map shows sporadic distribution with come cluster connectivity.

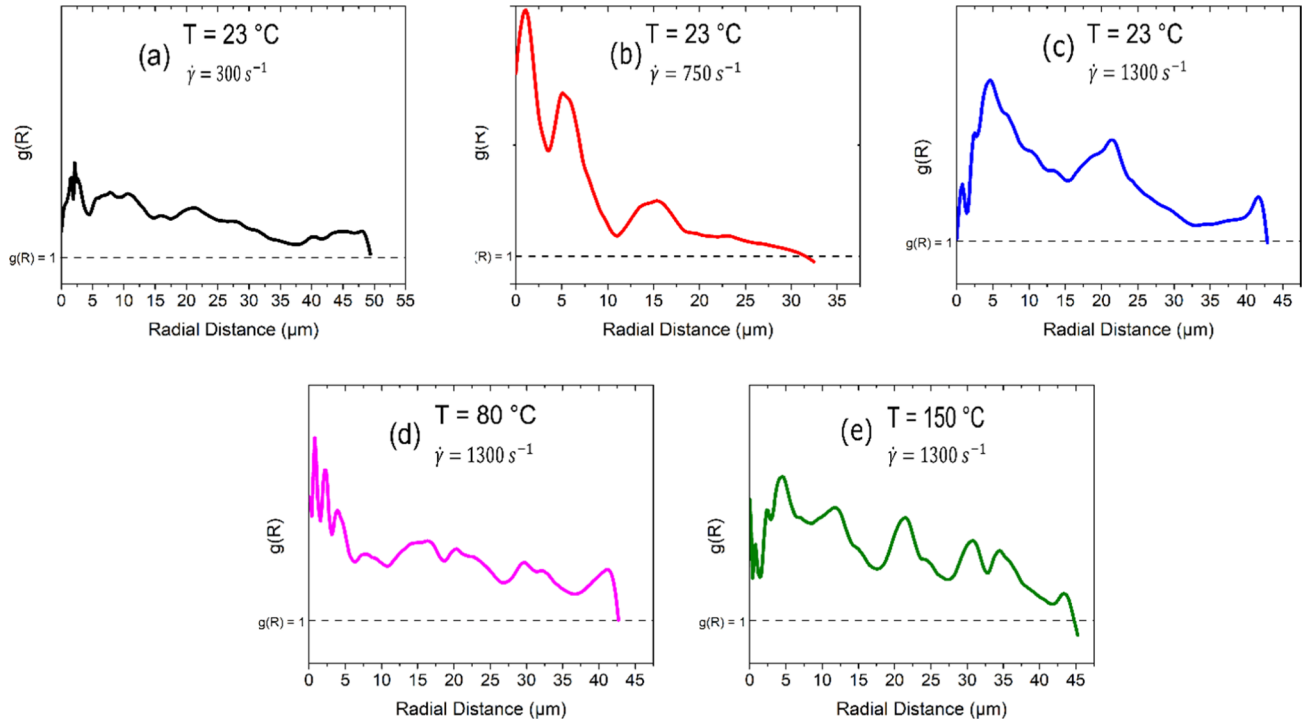


**Figure 4.** Radial distribution function coordinating carbon to manganese detections (a) 23 °C, 300 $s^{-1}$ shows minimal coordination (b) 23 °C, 750 $s^{-1}$ has primarily short-range contacts (c) 23 °C, 1300 $s^{-1}$ has large peaks for both short- and long-range connectivity (d) 80 °C, 1300 $s^{-1}$ has multiple peaks throughout large distances, suggesting more connectivity (e) 150 °C, 1300 $s^{-1}$ shows a strong presence of both short- and long-range connectivity.

active material, but analysis based on Co or Ni would yield identical results.

In this study, the reduced 2D map considers only the brightest pixel intensities and thus represents the top cross-section layer of the electrode (i.e., closest layer to the SEM detector). This is done through analyzing pixel intensity histograms, then setting a threshold to only include the highest intensity population. The highest intensity population is chosen to represent the surface elemental layer. The reduced 2D maps are then analyzed via 2D radial distribution functions between carbon/carbon (C/C) pixels and carbon/manganese (Mn/C) pixels. Two controls were performed to ensure that the radial distribution results were representative of the electrode film surface. Radial distribution functions were measured (1) as a function of EDS collection time and were found to be independent of time, and (2) at different spatial cross-sections of the same electrode and found to be independent of the sampled region. The results are shown in Figures S2 and S3, respectively. Control (2) in Figure S3 is considered a particularly important result, as it demonstrates that analysis of one EDS image of 100 $\mu$m × 150 $\mu$m is considered representative of the entire film. Even so, multiple cross-sections were analyzed under different experimental conditions (not shown) to ensure accuracy of the results. Figure S4a–c show radial distribution functions for C/C correlations for all low shear rate electrodes discussed in Figure 1. Interestingly, electrodes with very different performance, for example, 300 $s^{-1}$, 23 °C (Figure S4b) and 300 $s^{-1}$, 150 °C


https://dx.doi.org/10.1021/acsaem.0c01305
ACS Appl. Energy Mater. 2020, 3, 11681−11689

(Figure S4c), have very similar C/C radial distribution functions, that is, the overall electron conductivity is not limiting battery performance. This strongly supports the observations in Morelly et al., which showed similar in-plane film conductivity between high- and low-performing electrodes.[1]

Figure 4a–c shows the results of the Mn/C radial distribution function for low temperature (23 °C) films at three shear rates (300, 750, and 1300 $s^{-1}$). The value of $g(R)$ represents the probability that a C pixel is found within a certain distance of a Mn pixel.[35] Figure 4a shows one peak within 5 $\mu$m of any given Mn pixel. Because the average NMC radius is 5 $\mu$m, any peak before this distance indicates carbon directly in contact with the NMC particle surface (i.e., short-range contacts). Beyond 5 $\mu$m, $g(R)$ is relatively flat, which indicates a relatively random distribution of carbon.[36] Figure 4b shows a high concentration of C around a Mn pixel followed by a steep drop-off toward a random distribution around 20 $\mu$m. This radial distribution indicates primarily short-range Mn/C contacts, while Figure 4c indicates an increase in the order of Mn/C correlations at higher radial distances with distinct peaks at 5, 20, and 42 $\mu$m. Because electrode performance increases from Figure 4a,c, we therefore observe that the best performance correlates to the electrode with the highest short- and long-range C/Mn order. Figure 4b suggests that short-range order is better than the flat Mn/C $g(r)$ observed in Figure 4a. Together Figure 4c,b support the hypothesis that both short- and long-range C order with respect to NMC maximizes battery performance.

Figure 4c–e show the results for high shear (1300 $s^{-1}$) films at three drying temperatures (23, 80, and 150 °C). Recall that for all samples, different (at least two) cross sections of the same electrode were subjected to this analysis to ensure that these results are representative of a larger area of the electrode. Figure 4d indicates an initial high presence of C in direct contact with the active material surface, as well as multiple peaks of connectivity with increasing radial distance. Similarly, Figure 4e displays a multitude of peaks with increasing radial distance and similar magnitude with no significant drop in Mn/C probability for the entire range of distances. Figure 4c–e suggest that high shear rates induce short- and long-range order, creating shorter pathways for electrons and ions to come together. Figure 4d,e show very similar performance and have slightly higher discharge capacities than Figure 4c. Radial distribution functions have historically been used to determine the crystal lattice structure by identifying the number of nearest neighbors, and has since been adapted for use in amorphous solids.[36–38] Many mathematical models for other particle shapes have also been developed[39] and all suggest that this is a valid analysis of coordination by detecting nearest neighbors. Results that display multiple peaks correlate to a more highly ordered crystal structure,[36] and for this study, the "crystal structure" is defined as the C network, relative to Mn. Multiple peaks correlate to a higher Mn/C order in the form of short- and long-range contacts. The results in Figure 4c–e strongly support the hypothesis that short- and long-range Mn/C order leads to higher battery performance. However, the question remains why such vastly different structures arise from different shear and drying conditions.

It is known that the rheological response of battery slurries is primarily influenced by the conductive carbon additive network.[22,40] Figure S5 shows rheological characterization for the initial slurry used for all coating and drying conditions. The magnitude and frequency-independence of the storage ($G'$) and loss ($G''$) moduli indicate a strong colloidal gel with a spanning network of particles, consistent with previous findings.[1] We propose that the modulus as a function of time and processing history is a good indicator of carbon connectivity in the electrode slurry. For example, a decrease in modulus indicates a loss of carbon network connectivity and the formation of carbon islands (aggregates) throughout the electrode film. Therefore, we hypothesize that a correlation exists between modulus after shear and during drying and the radial distribution results observed in Figure 4. To this end, the effect of shear on the slurry structure is monitored by first applying a constant shear rate for a small strain, followed by a small amplitude oscillatory shear frequency sweep immediately after flow cessation. Figure 5 shows the results at room temperature of angular frequency sweeps at three times (0, 1, and 2 h) after exposure to (a) 300, (b) 750, and (c) 1300 $s^{-1}$.

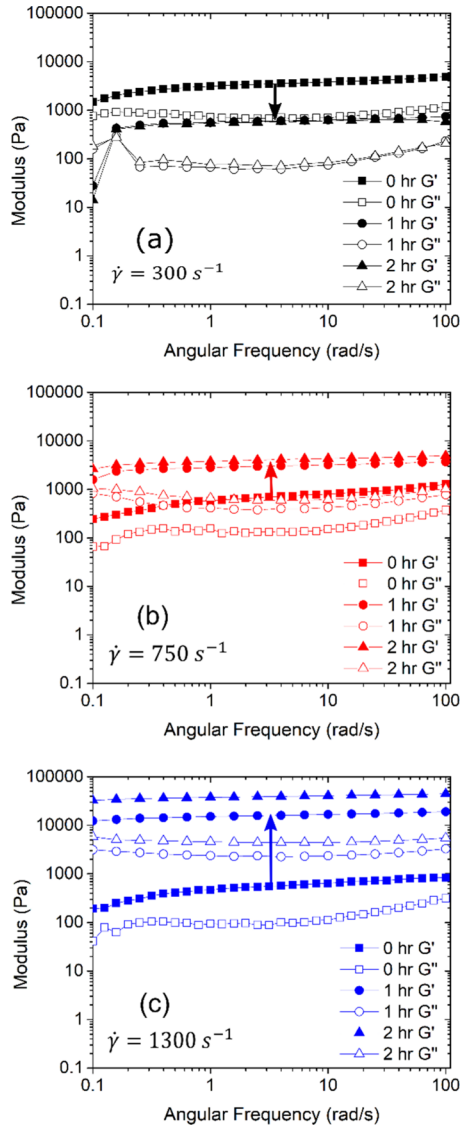


**Figure 5.** Time-dependent rheological response at room temperature after (a) 300 $s^{-1}$, where the decrease in moduli is caused by particle densification (b) 750 $s^{-1}$, observing an increase in moduli caused by particle dispersion (c) 1300 $s^{-1}$, showing immense increases related to high dispersion of carbon particles.


https://dx.doi.org/10.1021/acsaem.0c01305
ACS Appl. Energy Mater. 2020, 3, 11681–11689

The 0 h frequency sweep shows that 300 $s^{-1}$ has a structure similar to the structure measured before shearing (Figure S5) while 750 and 1300 $s^{-1}$ show significantly lower moduli than the starting structure. At low shear rates, Figure 5a shows that the modulus decreases with time, indicating a decrease in carbon-to-carbon network connectivity. However, for 750 and 1300 $s^{-1}$, the modulus increases with increasing time. This suggests that the carbon network is becoming more connected after exposure to high shear rates and less connected (forming dense aggregates) at low shear rates.

These results are in line with other reports in the literature. For example, the work by Eberle et al. defines a dimensionless value, $M' = \frac{6\pi\mu_s a^2\dot{\gamma}}{F_{max}}$ to relate shear forces to particle attraction forces. The results shown in Figure 5 can be explained if the hydrodynamic shear stresses are larger than the interparticle attractive forces, that is, $M' > 1$ for $\dot{\gamma} \geq 750$ $s^{-1}$ and smaller, that is, $M' < 1$, for $\dot{\gamma} = 300$ $s^{-1}$. Although measured on a different experimental system, Eberle showed that $M' < 1$ leads to the formation of dense clusters/aggregates and reduced network interconnectivity, while $M' > 1$ leads to increased network connectivity.[24] Furthermore, Colombo et al. show that gels exposed to low shear, for example, up to 100 $s^{-1}$, evolve to isotropic states with reduced moduli over 3000 s, or 50 min.[26] Coincidentally, similar timescales are observed in Figure 5a.

Figure 5 helps to explain the results in Figure 4a−c and suggest a correlation between carbon network connectivity and long-range order observed in battery electrodes. For example, Figures 5a and 4a ($\dot{\gamma} = 300$ $s^{-1}$) show the lowest carbon connectivity (via rheology) and the lowest Mn/C long-range order (via radial distribution function), respectively. Figures 5c and 4c ($\dot{\gamma} = 1300$ $s^{-1}$) show the highest carbon connectivity and highest Mn/C order, respectively. These strong correlations suggest that there is a critical shear rate for which battery slurries should be processed to ensure dispersion of carbon and connectivity between carbon and the active material. As previously mentioned, this shear rate is on the same order of magnitude as that applied during slot die coating, a process known to make better electrodes. The observed change in the microstructure at an increased shear rate could be responsible for the better performance of slot die coated electrodes.

Because the room temperature drying cases take up to 24 h to dry, the results of Figure 5 should be a realistic representation of the final slurry microstructure before drying at room temperature. At higher temperature, drying occurs much faster, and the results in Figure 5 may not represent the final structures. However, when the rate of drying is very fast, that is, 150 °C, the effect of structure reorganization is expected to be significantly reduced, and the structure immediately after flow cessation is more relevant. In fact, the lowest shear rate appears to have the highest electrode performance in Figure 1d. Figure 5a shows that the zero-hour structure for 300 $s^{-1}$ has the highest modulus and therefore highest carbon network connectivity. If we assume that at high drying rates this structure is locked into place, then the electrode should have both short- and long-range Mn/C orders. This is strongly supported by the radial distribution functions in Figure S6a,b, which show these correlations for the low shear rate dried at high temperature. These results support the importance of both temperature and shear on the final carbon dispersion with relation to the NMC particle surface, and strongly suggest that fast drying and no network reorganization is more effective at increasing discharge capacity than higher shear rates. The optimum temperature for drying will also need to consider physical properties, such as adhesion between the electrode and current collector as discussed in the works of Bauer, Schabel, and co-workers.[14,17,19]

## 4. CONCLUSIONS

A combination of electrochemical testing, rheological characterization, and EDS mapping with image analysis explains the effects of shear and drying temperature on the battery electrode microstructure and performance. Overall, the highest electrode discharge capacity is observed at high drying temperatures (150 °C) and high shear rates (1300 $s^{-1}$). Manganese (Mn) and carbon (C) connectivity, measured via the radial distribution function, correlates well with average discharge capacity. For example, higher shear rates at low drying temperatures lead to better long-range Mn/C orders and better battery performance, while high temperatures yield long-range Mn/C orders and better battery performance for all shear rates. The results clearly indicate that temperature is more important than the shear rate in achieving long-range Mn/C order, that is, better battery performance. This strongly supports the hypothesis that short and long-range order between the active material and conductive additive govern electrode performance. Additionally, there is an observed increased in electrode performance as the shear rate increases, which could explain the better performance of slot-die coated electrodes compared to electrodes made from lower shear rate blade coating.

The dependence of short- and long-range order on Mn/C distributions is best explained using rheology of the slurry after coating. Our findings, supported by the colloidal gel literature, show that too low of a shear rate during coating can lead to densification of the microstructure and a loss of long-range Mn/C order. The resulting loss of Mn/C correlations inhibits electron transport and consequently decreases discharge capacity. For higher shear rates, the slurry microstructure shows increased carbon connectivity and higher long-range Mn/C order. The effects of microstructural changes after shear are minimized with increased drying temperature, which locks the sheared structure in place. These results clearly indicate the importance of the slurry microstructure during coating and drying and are expected to depend on the starting slurry microstructure.

To our knowledge, this work is the first study to correlate the underlying elemental connectivity to battery performance as a function of shear and temperature. The radial distribution function applied to EDS elemental maps is an effective method to quantify short- and long-range contacts in battery electrodes. This method should prove useful in future studies to correlate processing conditions to battery performance.

## ■ ASSOCIATED CONTENT

### Supporting Information

The Supporting Information is available free of charge at https://pubs.acs.org/doi/10.1021/acsaem.0c01305.

Full account of battery cycling data; effects of EDS exposure time on the radial distribution functions after thresholding; results of radial distribution functions for multiple analysis areas of the same electrode to validate conclusions; C/C radial distribution function results;



https://dx.doi.org/10.1021/acsaem.0c01305
ACS Appl. Energy Mater. 2020, 3, 11681−11689

rheological frequency sweep of initial slurry structure; and C/Mn coordination for increased drying temperature (PDF)

## AUTHOR INFORMATION


### Corresponding Author

**Nicolas J. Alvarez** − *Department of Chemical and Biological Engineering, Drexel University, Philadelphia, Pennsylvania 19104, United States;* orcid.org/0000-0002-0976-6542; Email: nja49@drexel.edu

### Authors

**Renee M. Saraka** − *Department of Chemical and Biological Engineering, Drexel University, Philadelphia, Pennsylvania 19104, United States*

**Samantha L. Morelly** − *Department of Chemical and Biological Engineering, Drexel University, Philadelphia, Pennsylvania 19104, United States*

**Maureen H. Tang** − *Department of Chemical and Biological Engineering, Drexel University, Philadelphia, Pennsylvania 19104, United States;* orcid.org/0000-0003-0037-4814

Complete contact information is available at: https://pubs.acs.org/10.1021/acsaem.0c01305


### Author Contributions

R.M.S. performed all coating, drying, rheology, imaging and battery testing measurements. S.L.M. fabricated the coin cells for battery testing. R.M.S. wrote the first draft of the manuscript. All authors contributed to manuscript edits. All authors have given approval to the final version of the manuscript.


### Funding

NSF CBET-1929755.


### Notes

The authors declare no competing financial interest.

## ACKNOWLEDGMENTS


R.M.S. and N.J.A. would like to thank Cameron Abrams for helpful discussions regarding the application of the radial distribution function to EDS elemental maps.


## REFERENCES


(1) Morelly, S. L.; Alvarez, N. J.; Tang, M. H. Short-Range Contacts Govern the Performance of Industry-Relevant Battery Cathodes. *J. Power Sources* **2018**, *387*, 49−56.

(2) Peterson, S. W.; Wheeler, D. R. Direct Measurements of Effective Electronic Transport in Porous Li-Ion Electrodes. *J. Electrochem. Soc.* **2014**, *161*, A2175−A2181.

(3) Bockholt, H.; Indrikova, M.; Netz, A.; Golks, F.; Kwade, A. The Interaction of Consecutive Process Steps in the Manufacturing of Lithium-Ion Battery Electrodes with Regard to Structural and Electrochemical Properties. *J. Power Sources* **2016**, *325*, 140−151.

(4) Dominko, R.; Gaberšček, M.; Drofenik, J.; Bele, M.; Jamnik, J. Influence of Carbon Black Distribution on Performance of Oxide Cathodes for Li Ion Batteries. *Electrochim. Acta* **2003**, *48*, 3709−3716.

(5) Dominko, R.; Gaberscek, M.; Drofenik, J.; Bele, M.; Pejovnik, S.; Jamnik, J. The Role of Carbon Black Distribution in Cathodes for Li Ion Batteries. *J. Power Sources* **2003**, *119*−*121*, 770−773.

(6) Zheng, H.; Yang, R.; Liu, G.; Song, X.; Battaglia, V. S. Cooperation between Active Material, Polymeric Binder and Conductive Carbon Additive in Lithium Ion Battery Cathode. *J. Phys. Chem. C* **2012**, *116*, 4875−4882.

(7) Cerbelaud, M.; Lestriez, B.; Videcoq, A.; Ferrando, R.; Guyomard, D. Understanding the Structure of Electrodes in Li-Ion Batteries: A Numerical Study. *J. Electrochem. Soc.* **2015**, *162*, A1485−A1492.

(8) Kraytsberg, A.; Ein-Eli, Y. Conveying Advanced Li-Ion Battery Materials into Practice The Impact of Electrode Slurry Preparation Skills. *Adv. Energy Mater.* **2016**, *6*, 1600655.

(9) Mohanty, D.; Hockaday, E.; Li, J.; Hensley, D. K.; Daniel, C.; Wood, D. L. Effect of Electrode Manufacturing Defects on Electrochemical Performance of Lithium-Ion Batteries: Cognizance of the Battery Failure Sources. *J. Power Sources* **2016**, *312*, 70−79.

(10) Yoo, M.; Frank, C. W.; Mori, S. Interaction of Poly(Vinylidene Fluoride) with Graphite Particles. 1. Surface Morphology of a Composite Film and Its Relation to Processing Parameters. *Chem. Mater.* **2003**, *15*, 850−861.

(11) Yoo, M.; Frank, C. W.; Mori, S.; Yamaguchi, S. Interaction of Poly(Vinylidene Fluoride) with Graphite Particles. 2. Effect of Solvent Evaporation Kinetics and Chemical Properties of PVDF on the Surface Morphology of a Composite Film and Its Relation to Electrochemical Performance. *Chem. Mater.* **2004**, *16*, 1945−1953.

(12) Nanjundaswamy, K. S.; Friend, H. D.; Kelly, C. O.; Standlee, D. J.; Higgins, R. L. Electrode Fabrication for Li-Ion: Processing, Formulations and Defects during Coating. *IECEC-97 Proceedings of the Thirty-Second Intersociety Energy Conversion Engineering Conference (Cat. No. 97CH6203)*, 1997; Vol. *1*, pp 42−45.

(13) Hawley, W. B.; Li, J. Electrode Manufacturing for Lithium-Ion Batteries—Analysis of Current and next Generation Processing. *J. Energy Storage* **2019**, *25*, 100862.

(14) Bitsch, B.; Dittmann, J.; Schmitt, M.; Scharfer, P.; Schabel, W.; Willenbacher, N. A Novel Slurry Concept for the Fabrication of Lithium-Ion Battery Electrodes with Beneficial Properties. *J. Power Sources* **2014**, *265*, 81−90.

(15) Lee, G.-W.; Ryu, J. H.; Han, W.; Ahn, K. H.; Oh, S. M. Effect of Slurry Preparation Process on Electrochemical Performances of LiCoO2 Composite Electrode. *J. Power Sources* **2010**, *195*, 6049−6054.

(16) Susarla, N.; Ahmed, S.; Dees, D. W. Modeling and Analysis of Solvent Removal during Li-Ion Battery Electrode Drying. *J. Power Sources* **2018**, *378*, 660−670.

(17) Müller, M.; Pfaffmann, L.; Jaiser, S.; Baunach, M.; Trouillet, V.; Scheiba, F.; Scharfer, P.; Schabel, W.; Bauer, W. Investigation of Binder Distribution in Graphite Anodes for Lithium-Ion Batteries. *J. Power Sources* **2017**, *340*, 1−5.

(18) Westphal, B. G.; Kwade, A. Critical Electrode Properties and Drying Conditions Causing Component Segregation in Graphitic Anodes for Lithium-Ion Batteries. *J. Energy Storage* **2018**, *18*, 509−517.

(19) Jaiser, S.; Müller, M.; Baunach, M.; Bauer, W.; Scharfer, P.; Schabel, W. Investigation of Film Solidification and Binder Migration during Drying of Li-Ion Battery Anodes. *J. Power Sources* **2016**, *318*, 210−219.

(20) Schmitt, M.; Scharfer, P.; Schabel, W. Slot Die Coating of Lithium-Ion Battery Electrodes: Investigations on Edge Effect Issues for Stripe and Pattern Coatings. *J. Coat. Technol. Res.* **2014**, *11*, 57−63.

(21) Gutoff, E. B.; Cohen, E. D. *Coating and Drying Defects: Troubleshooting Operating Problems*; John Wiley & Sons, 2006.

(22) Bauer, W.; Nötzel, D. Rheological Properties and Stability of NMP Based Cathode Slurries for Lithium Ion Batteries. *Ceram. Int.* **2014**, *40*, 4591−4598.

(23) Russel, W. B.; Saville, D. A.; Schowalter, W. R. *Colloidal Dispersions*; Press, Cambridge, 1989 (accessed Apr 21, 2020).

(24) Eberle, A. P. R.; Martys, N.; Porcar, L.; Kline, S. R.; George, W. L.; Kim, J. M.; Butler, P. D.; Wagner, N. J. Shear Viscosity and Structural Scalings in Model Adhesive Hard-Sphere Gels. *Phys. Rev. E: Stat., Nonlinear, Soft Matter Phys.* **2014**, *89*, 050302.

(25) Martys, N. S.; Khalil, M.; George, W. L.; Lootens, D.; Hébraud, P. Stress Propagation in a Concentrated Colloidal Suspension under Shear. *Eur. Phys. J. E* **2012**, *35*, 20.

(26) Colombo, G.; Kim, S.; Schweizer, T.; Schroyen, B.; Clasen, C.; Mewis, J.; Vermant, J. Superposition Rheology and Anisotropy in

Rheological Properties of Sheared Colloidal Gels. *J. Rheol.* **2017**, *61*, 1035−1048.
(27) Varadan, P.; Solomon, M. J. Shear-Induced Microstructural Evolution of a Thermoreversible Colloidal Gel. *Langmuir* **2001**, *17*, 2918−2929.
(28) Gordon, M. B.; Kloxin, C. J.; Wagner, N. J. The Rheology and Microstructure of an Aging Thermoreversible Colloidal Gel. *J. Rheol.* **2017**, *61*, 23−34.
(29) López-Barrón, C. R.; Gurnon, A. K.; Eberle, A. P. R.; Porcar, L.; Wagner, N. J. Microstructural Evolution of a Model, Shear-Banding Micellar Solution during Shear Startup and Cessation. *Phys. Rev. E: Stat., Nonlinear, Soft Matter Phys.* **2014**, *89*, 042301.
(30) Hipp, J. B.; Richards, J. J.; Wagner, N. J. Structure-Property Relationships of Sheared Carbon Black Suspensions Determined by Simultaneous Rheological and Neutron Scattering Measurements. *J. Rheol.* **2019**, *63*, 423−436.
(31) Hoekstra, H.; Vermant, J.; Mewis, J.; Fuller, G. G. Flow-Induced Anisotropy and Reversible Aggregation in Two-Dimensional Suspensions. *Langmuir* **2003**, *19*, 9134−9141.
(32) Morelly, S. L.; Gelb, J.; Iacoviello, F.; Shearing, P. R.; Harris, S. J.; Alvarez, N. J.; Tang, M. H. Three-Dimensional Visualization of Conductive Domains in Battery Electrodes with Contrast-Enhancing Nanoparticles. *ACS Appl. Energy Mater.* **2018**, *1*, 4479−4484.
(33) Shindo, D.; Oikawa, T. Energy Dispersive X-Ray Spectroscopy. In *Analytical Electron Microscopy for Materials Science*; Shindo, D., Oikawa, T., Eds.; Springer Japan: Tokyo, 2002; pp 81−102.
(34) Allen, M. P.; Tildesley, D. J. Computer Simulation of Liquids (Oxford Science Publications): 9780198556459: Amazon.com: Books https://www.amazon.com/Computer-Simulation-Liquids-Science-Publications/dp/0198556454 (accessed April 27, 2020).
(35) Brostow, W. Radial Distribution Function Peaks and Coordination Numbers in Liquids and in Amorphous Solids. *Chem. Phys. Lett.* **1977**, *49*, 285−288.
(36) Harper, R. A.; Posner, A. S. Radial Distribution Study of Non-Crystalline Tricalcium Phosphate. *Mater. Res. Bull.* **1970**, *5*, 129−136.
(37) Srolovitz, D.; Egami, T.; Vitek, V. Radial Distribution Function and Structural Relaxation in Amorphous Solids. *Phys. Rev. B* **1981**, *24*, 6936−6944.
(38) Li, F.; Lannin, J. S. Radial Distribution Function of Amorphous Carbon. *Phys. Rev. Lett.* **1990**, *65*, 1905−1908.
(39) Root, L. J.; Lovett, R. On the Interpretation of Radial Distribution Functions Determined from Integral Equations. *J. Chem. Phys.* **1991**, *95*, 8390−8397.
(40) Morelly, S. L.; Tang, M. H.; Alvarez, N. J. The Impotence of Non-Brownian Particles on the Gel Transition of Colloidal Suspensions. *Polymers* **2017**, *9*, 461.


https://dx.doi.org/10.1021/acsaem.0c01305
*ACS Appl. Energy Mater.* 2020, 3, 11681−11689